Thermal conductance of carbon nanotube contacts: Molecular dynamics simulations and general description of the contact conductance

Richard N. Salaway[1] and Leonid V. Zhigilei[2,*]

[1]*Department of Mechanical and Aerospace Engineering, University of Virginia, 122 Engineers Way, Charlottesville, Virginia 22904-4746, USA*

[2]*Department of Materials Science and Engineering, University of Virginia, 395 McCormick Road, Charlottesville, Virginia 22904-4745, USA*

(Received 23 December 2015; revised manuscript received 1 June 2016; published 15 July 2016)

The contact conductance of carbon nanotube (CNT) junctions is the key factor that controls the collective heat transfer through CNT networks or CNT-based materials. An improved understanding of the dependence of the intertube conductance on the contact structure and local environment is needed for predictive computational modeling or theoretical description of the effective thermal conductivity of CNT materials. To investigate the effect of local structure on the thermal conductance across CNT-CNT contact regions, nonequilibrium molecular dynamics (MD) simulations are performed for different intertube contact configurations (parallel fully or partially overlapping CNTs and CNTs crossing each other at different angles) and local structural environments characteristic of CNT network materials. The results of MD simulations predict a stronger CNT length dependence present over a broader range of lengths than has been previously reported and suggest that the effect of neighboring junctions on the conductance of CNT-CNT junctions is weak and only present when the CNTs that make up the junctions are within the range of direct van der Waals interaction with each other. A detailed analysis of the results obtained for a diverse range of intertube contact configurations reveals a nonlinear dependence of the conductance on the contact area (or number of interatomic intertube interactions) and suggests larger contributions to the conductance from areas of the contact where the density of interatomic intertube interactions is smaller. An empirical relation accounting for these observations and expressing the conductance of an arbitrary contact configuration through the total number of interatomic intertube interactions and the average number of interatomic intertube interactions per atom in the contact region is proposed. The empirical relation is found to provide a good quantitative description of the contact conductance for various CNT configurations investigated in the MD simulations and is suitable for incorporation into mesoscopic models capable of predicting the effective thermal transport properties of CNT materials.

DOI: 10.1103/PhysRevB.94.014308

I. INTRODUCTION

As simultaneous reduction in size and increase in power levels of microelectronic devices generate higher heat flux densities, the development of advanced thermal management systems becomes critical [1]. Carbon nanotubes (CNTs) have gained a significant amount of research interest for use in thermal management applications due to exceptionally high values of the intrinsic thermal conductivity of individual CNTs, k, reported in experiments [2–9] and computational studies [10–30]. Specific examples of the use of CNTs to enhance the efficiency of heat sinks or heat dissipation to the surrounding environment include the efficient cooling of silicon chips by CNT microfin structures [31], the use of CNT bumps in high-frequency, high-power, flip-chip amplifiers [32], and the design of CNT-based thermal interface materials (TIMs) [33–43].

Despite the high intrinsic thermal conductivity of individual CNTs, the values of the effective conductivity reported for CNT-based materials are often relatively low and exhibit large variability [44–51]. The weak thermal coupling between the CNTs, defined by nonbonding van der Waals interactions, is commonly assumed to be the limiting factor that controls the thermal transport in the CNT materials [51–58]. Indeed, the results of recent molecular dynamics (MD) simulations [59] suggest that intertube interactions have negligible effect on the intrinsic conductivity of individual CNTs. This observation implies that the effective conductivity of CNT materials is largely defined by the intrinsic CNT conductivity, k, the characteristics of intertube conductance, and the arrangement of the CNTs in the material. With the values of k being successfully elucidated in atomistic modeling and experiments [2–30], and the general scaling laws governing the effective conductivity of CNT network materials being revealed in the mesoscopic modeling and theoretical analysis [59–62], the uncertainty in the dependence of the intertube conductance on the density and geometrical characteristics of the CNT-CNT contacts presents a remaining stumbling block in the way of establishing a clear quantitative description of the thermal conductivity of CNT materials. A brief overview of the results of experimental and computational studies of the intertube contact conductance reported so far is provided below.

The only direct experimental measurements of thermal conductance between individual CNTs reported to date are the ones obtained for multiwalled CNTs by Yang *et al.* [52,63]. The results of these studies suggest that the interfacial conductance per unit area has a strong dependence on the geometry of the contact (the conductance per unit area is about an order of magnitude lower for CNTs that are aligned with each other at the contact as compared to the CNTs crossing each other at an angle) [52], as well as the diameter of the

*Corresponding author: lz2n@virginia.edu

CNTs (the conductance per unit area exhibits a close to linear increase with the tube diameter) [63]. While the latter dependence has been discussed in terms of the characteristics of the intershell phonon transport in the multiwalled CNTs [63], the former observation suggests a strong sensitivity of the effective thermal conductivity of CNT materials to their structural organization. It also puts into question the reliability of the estimations of the intertube contact conductance based on the experimental values of the effective conductivity of CNT materials [47,51,64,65]. These estimations typically rely on analytical equations derived for idealized systems composed of randomly dispersed straight nanotubes [57,60,62,66], whereas the arrangement of CNTs into bundles in real CNT materials has been shown to have a dramatic effect on the intertube heat exchange and the effective thermal conductivity [60,62].

Given the difficulties in obtaining the complete picture of the intertube heat transfer from experimental data, computational analysis based on MD simulations has been playing the leading role in advancing the physical understanding of the thermal transport across CNT-CNT contacts [51,53–56,58,67–69]. With complete characterization of the physical system being studied, the MD simulation method allows for a systematic study of the dependence of CNT-CNT conductance on parameters that may be modified to optimize the thermal properties of CNT-based materials. The simulations have provided important insights into the mechanisms responsible for the intertube heat transfer between parallel CNTs [53–56] or CNTs crossing each other at an angle [51,58,67–69]. While the variation of the values of the conductance per unit area of the intertube contacts by more than two orders of magnitude [56] suggests a strong and complex dependence of the intertube conductance on the geometry and density of the contacts, the design of a general heat transfer model that would account for this dependence is hampered by the differences in computational methods, interatomic potentials, definitions of the contact area, length, and type of the CNTs used in the simulations, etc. A brief discussion of some of the factors affecting the simulation results is provided below.

A length dependence of the thermal conductivity of individual CNTs is commonly observed in MD simulations [13,15,22–24,27,70]. While much of this length dependence can be attributed to an increase of ballistic thermal transport length as CNT length increases in the ballistic length regime, Cao and Qu [29] argued that an increase in available long-wavelength phonon states with increasing CNT length also contributes significantly to the increase in conductivity. It is plausible that the addition of long-wavelength phonon states may also promote an increase in CNT-CNT conductance if these phonons contribute to the conductance. Kumar and Murthy [67] employed MD simulations to perform wavelet analysis of thermal pulse propagation along the axes of CNTs forming perpendicular cross-junctions at a very low temperature (0.01 K). The wavelet traveled along the axis of one CNT and passed through the contact region into the second perpendicular CNT. Analysis of the vibrational frequencies showed that most of the dominant frequencies excited in the second CNT were relatively low (less than 10 THz), implying that low-frequency, long-wavelength phonons transmit across CNT-CNT junctions more readily. Though there have been several direct MD investigations into the length dependence of CNT-CNT conductance, a definitive and consistent description is still lacking. Evans *et al.* [58] performed MD simulations of conductance at a junction between two perpendicular (10,10) CNTs and found a significant length effect up to CNT lengths of about 20 nm. In similar simulations by Hu and McGaughey [71] the strong length dependence of the intertube conductance is observed for (6,6) CNTs with length of up to 75 nm. Zhong and Lukes [53] simulated the conductance between parallel, overlapping CNTs with varying overlap and CNT length. They showed a pronounced length dependence below 10 nm, which becomes weaker as the CNT length reaches 40 nm. Xu and Buehler [55] also modeled the conductance between parallel CNTs and reported only very weak length dependence for CNTs between 25 and 75 nm.

While these results are not in direct contradiction with each other, there are still unresolved issues regarding the length dependence of CNT-CNT conductance. The works referenced above considered either only parallel CNTs or CNT cross junctions and did not attempt to come up with a general description of CNT-CNT conductance applicable to different configurations. A broader range of CNT lengths should be examined to definitively determine the saturation limit of CNT length effects. Important aspects to discern include the strength of this length dependence and the range of CNT lengths for which it is present. Therefore a series of simulations was performed to investigate the effect of CNT length on CNT-CNT conductance and the results of this study are presented in Sec. III B.

The thermal conductivity of CNT-based materials can be increased by increasing the density of CNTs. Evans and Keblinski [68] performed MD simulations of thermal conductivity through repeated layers of perpendicular CNT arrays. They reported the thermal conductivity of a stacked crossbar structure consisting of four CNTs per repeated layer to be four times greater than that of a structure consisting of two CNTs per layer. Despite these results, it is possible that an increase in contact density may not always increase the total conductivity in a CNT based material. Prasher *et al.* [51] employed atomistic Green's function simulations to model thermal conductance across individual junctions formed by perpendicular CNTs. They compared the conductance per junction for the case of a single junction formed by two perpendicular CNTs to the conductance per junction for the case of two junctions formed when two parallel CNTs were crossed by a single perpendicular CNT, to study the effects of contact density on the conductance per junction. Their results show that the conductance per junction is reduced by approximately an order of magnitude for the two junction case, when the junctions are separated by only 0.816 nm. It follows that for some configurations, an increase in contact density may impede the overall thermal transport through the CNT network. In fact, the authors cite the decreased conductance per junction as the main explanation of discrepancies between the results of their experimental measurements of conductivity of a CNT bed and an analytical equation [57] derived for a random network of straight CNTs. Although the analytical equation has since been corrected [60,66], an even larger reduction of the contact conductance (by more than three orders of magnitude) would be required to reconcile the predictions of the corrected analytical equation with experimental data [60]. Thus it is important

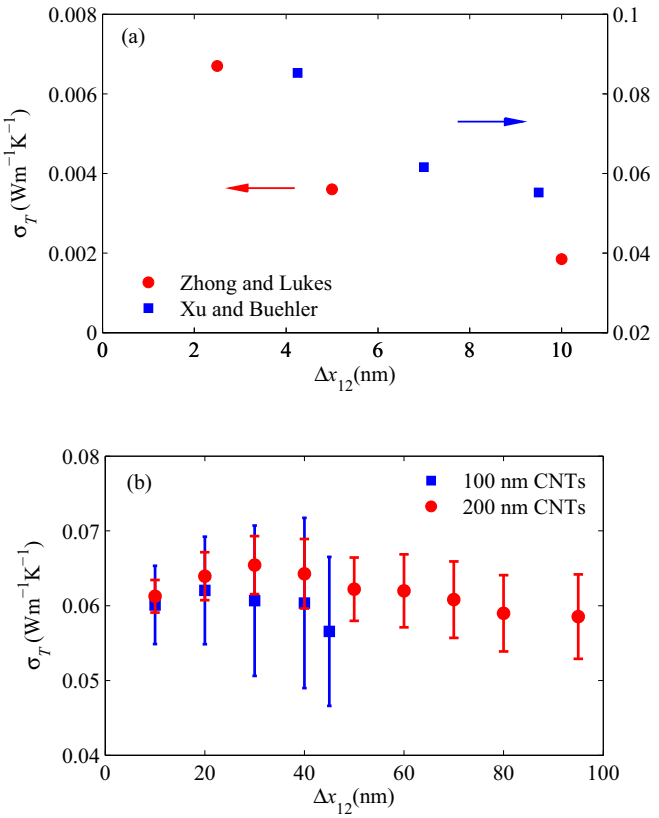

FIG. 1. A comparison of the values of CNT-CNT conductance per unit length predicted for different overlap lengths in (a) two studies of overlapping CNTs with $\Delta x_{12} \leqslant 10$ nm by Zhong and Lukes [53] and Xu and Buehler [55], and (b) a study of overlapping CNTs with $\Delta x_{12} \geqslant 10$ nm by Volkov *et al.* [59]. The values presented in (a) have been manipulated from the original references to reflect conductance per overlap length. Results of both works with $\Delta x_{12} \leqslant 10$ nm show an inverse relationship between conductance per area and contact area, while results of the study with $\Delta x_{12} \geqslant 10$ nm demonstrate the conductance per area to be independent of contact area.

to resolve any uncertainty regarding the influence of contact density on individual contact conductance. To this end, a series of simulations was performed to resolve the relationship between contact density and CNT-CNT conductance. The results of these simulations are reported in Sec. III C.

Defining an intertube contact area for an arbitrary configuration of neighboring CNTs is a nontrivial task, which leads to the lack of uniformity in the definitions used in different studies. However, in the case of parallel, overlapping CNTs, as studied in some of the works referenced above [53,55,59], any realistic definition should yield the contact area that is linearly proportional to Δx_{12}, the length of the overlapping region between the two CNTs. Moreover, the contact conductance can be defined as the conductance *per overlap length*, σ_T, given in W m^{-1} K^{-1} and linearly proportional to the conductance per area. Thus the effect of contact area on conductance per area can be indirectly observed by varying Δx_{12} and studying the effect of this variation on σ_T.

When the results from the previous works are defined in this manner, an interesting observation emerges. Figure 1(a) represents the data from two studies of overlapping CNTs with overlap lengths $\leqslant 10$ nm. Here, the data have been manipulated from the original form in the cited works to represent the conductance per overlap length, σ_T. In both sets of data, σ_T is observed to decrease with increasing Δx_{12}. These observations imply that conductance per area *decreases* with increasing contact area over the range of overlap lengths studied.

In contrast, the results of a study by Volkov *et al.* [59] shown in Fig. 1(b), demonstrate that the conductance per area is independent of the contact area when the CNT-CNT overlaps are longer than 10 nm. A close to linear variation of contact conductance with contact area is also reported in investigations performed for pairs of CNTs crossing each other at different angles [58,71]. The summation of these results suggests that the dependence of conductance per area on contact area may differ for different contact areas and different geometries/types of the contacts. In order to provide a better understanding of the effect of contact area on conductance across CNT-CNT contacts, a series of simulations for CNT configurations with different contact areas was designed and the results of the simulations are presented in Sec. III D.

The summation of the computational results obtained for various types of CNT-CNT contacts is used to formulate a general model that captures the dependence of the CNT-CNT contact conductance on the characteristics of local configurations of the interacting nanotubes in the contact region. This general model, described in Sec. IV, is based on the assumption that the contribution from individual interatomic intertube interactions to the CNT-CNT conductance decreases as the density of interatomic interactions across the contact increases. The predictions of the model are related to the results of the MD simulations and a good agreement is demonstrated for all intertube contact configurations. Finally, the results of this work are summarized in Sec. V.

II. COMPUTATIONAL MODEL

Several series of simulations are performed to investigate the effect of the local structure on the thermal conductance across CNT-CNT interfaces. All simulations are performed for single-walled (10,10) CNTs, that have been used in many of the earlier studies of intertube contact conductance [51,53,55,58,68]. This choice of the model system makes it easier to relate the results of the present study to the earlier computational predictions. While the computational details vary between the series, some aspects are common to all simulations presented in this paper and are described in this section as the general computational procedure. Any modifications made to this general computational procedure for any of the simulation series are explicitly noted when the corresponding results are presented. The Tersoff potential [72] describes interactions between carbon atoms belonging to the same CNT, and the 12-6 form of the LJ potential [73] describes the nonbonded van der Waals interactions between atoms belonging to different CNTs. In this implementation, the LJ parameters are $\sigma = 3.41$ Å and $\epsilon = 3.0$ meV. These values were chosen to closely match the values obtained through private communications with Evans *et al.*, who conducted a similar study [58] of the length dependence of CNT-CNT

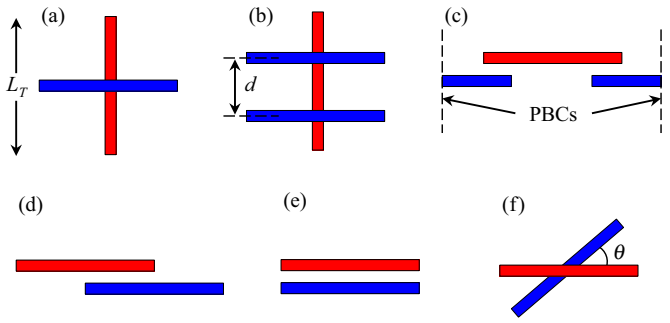

FIG. 2. Schematic representations of the simulation configurations employed in this work. The simulations were performed for (a) perpendicular CNT cross junctions with CNT length L_T, (b) two perpendicular CNT cross junctions with separation distance d, (c) parallel, partially overlapping CNTs with periodic boundary conditions (PBCs), (d) parallel, partially overlapping CNTs with free boundary conditions, (e) parallel, fully overlapping CNTs, and (f) CNT cross junctions with varying angle θ.

conductance and an additional study [68] of the effect of contact density on CNT-CNT conductance, for the sake of comparison. A cutoff distance is applied to ensure the LJ potential equals zero for separation distances greater than 1 nm. The equations of motion are solved using the velocity Verlet algorithm and the timestep of integration is 1 fs. All simulations described in this paper were performed with the large-scale atomic/molecular massively parallel simulator (LAMMPS) package [74].

Schematic representations of the various simulation configurations employed in this work are presented in Fig. 2. The details of each configuration are provided with the computational results in Sec. III. Initially, configurations are relaxed by quenching atomic velocities for 0.25 or 0.5 ns, depending on the configuration, to establish an equilibrium separation between the nanotubes and to prevent nonthermal oscillations that would affect intertube interactions. In the case of periodic boundary conditions, the dimensions of the computational cell are gradually adjusted at this stage to reach a target pressure of 1 atm in the directions in which the periodic boundaries are applied. The temperature of each CNT is determined from

$$T_l = \frac{1}{3k_B N_l} \sum_{i \in l} m_i v_i^2, \tag{1}$$

where T_l is the temperature of CNT l, N_l is the number of atoms in CNT l, v_i is the instantaneous velocity of atom i, m_i is the atomic mass, k_B is the Boltzmann constant, and the summation is performed over all atoms in CNT l. The relaxed/quenched systems are then gradually heated to 300 K by applying the Langevin thermostat [75] for 0.25 or 0.5 ns, depending on the configuration. In the case of periodic boundary conditions, the sizes of the computational cell are gradually adjusted again to reach the target pressure of 1 atm for the final simulation temperature of 300 K.

Thermal management is applied to each tube in its entirety, which introduces smaller perturbations to the equilibrium phonon distributions as compared to the alternative local heat bath implementations. Energy is added to one CNT at a rate of Q_{HB} by scaling the velocities of all atoms in the CNT, while energy is removed from a neighboring CNT at a rate of $-Q_{\mathrm{HB}}$ by the same method. In this way, a flux is created across the junction from one CNT to the neighboring CNT with a heat flow rate of Q_{HB}. This results in a temperature difference between the two tubes, ΔT_{12}. This temperature difference increases with simulation time, until a steady-state temperature difference is achieved, which is related to the applied heat flux Q_{HB} and CNT-CNT conductance G by the expression $G = Q_{\mathrm{HB}}/\Delta T_{12}$. The values of the heat flux are chosen so that the temperature difference between the CNTs is approximately 100 K, which is found to ensure independence of the predicted thermal conductance on the applied flux.

The lengths of the CNTs investigated in this study range from 5 to 200 nm, with the number of atoms per tube ranging from 800 to 31 560 for 5- and 200-nm tubes, respectively. Due to statistical anomalies arising from the velocity scaling of a limited number of atoms, the scaling procedure may result, over time, in a net momentum acquired by individual tubes, leading to a slide of the point of contact between the two tubes along the axis of one or both of the tubes. To prevent an individual tube from acquiring a nonzero net momentum, a small spring force is applied to each tube to restore it back to it's original position. The spring force is applied evenly to all atoms in the tube, and the net magnitude of the force in the ith direction is $F_i = -K_{\mathrm{Spr}}\Delta x_i$, where Δx_i is the difference between ith coordinates of the tube's current center of mass position and its initial center of mass position, and $K_{\mathrm{Spr}} = 0.0003$ eV Å^{-2} is the spring constant. This value of the spring constant is chosen such that the spring potential, $U_i = 0.5K_{\mathrm{Spr}}{\Delta x_i}^2$, is equal to $k_B T$ at $\Delta x_i = 14$ Å, where T is the system temperature of 300 K, and 14 Å is roughly equal to the tube diameter. In this way, small, random perturbations about equilibrium, associated with the thermal vibrations of the system, are not suppressed, while larger nonphysical displacements are prevented. The spring implementation was validated by performing two identical simulations with the exception of implementing the spring in one and excluding it from the other. No statistically relevant difference was found between the final results of the two methods. Therefore it also follows that no statistically significant effect is introduced when a nonzero momentum of individual tubes is present. Nonetheless, the spring implementation is adopted in the simulations for ease of visualization and data interpretation.

Due to the high intrinsic thermal conductivity of CNTs (the thermal resistance of an intertube contact is equivalent to the thermal resistance of a CNT with length of a few tens of micrometers [62]), the temperature variation along the CNTs is virtually absent in the simulations. Therefore the average temperature of each CNT is calculated by evaluating Eq. (1) over all atoms in a CNT, and the temperature difference ΔT_{12} is defined as the difference between the two nanotubes. A time series is generated by recording the average temperature of each CNT every 1 fs during the simulation. A moving average of each CNT's temperature is then generated by averaging each time series over a 40 or 50 ps temporal window, depending on the simulation series, to reduce statistical noise. A moving average of G is calculated over the same temporal window from the constant applied flux Q_{HB} and a moving average of ΔT_{12}, which is the difference between the moving average

temperatures of the two CNTs that are in contact with each other. This moving average of G approaches and eventually fluctuates about, a constant value when the system reaches the steady state. The time required to reach the steady state ranges from ∼2 to ∼30 ns, depending on the system size, the applied flux, and the simulation configuration. After steady state has been achieved, the moving average of G is recorded for an additional period of 1 to 6 ns, depending on the system size and the corresponding level of statistical noise, to generate a sample set of G measurements. The mean of this sample set is the final reported value of G, and the sample standard deviation is taken as a measure of variation in the final value.

III. COMPUTATIONAL RESULTS

A. Effect of overlap length

Two series of simulations are performed to investigate the effect of overlap length on the conductance between parallel, overlapping CNTs. In the first series, nonequilibrium MD (NEMD) simulations are performed to predict the thermal conductance at the interface between two partially overlapping parallel CNTs. The general geometric arrangement of the CNTs is identical to the one used in the simulations described in a previous work [59] and is depicted in the schematic shown in Fig. 3(a). Two parallel (10,10) CNTs of equal length, L_T, are orientated along the x axis. Free boundary conditions are applied in the y and z directions, and periodic boundary conditions are applied in the x direction. The CNTs are arranged such that two contacts with overlap length Δx_{12} are formed. Five independent configurations are constructed this way, for $L_T = 100$ nm, $\Delta x_{12} = 10$, 20, 30, 40 nm, and $L_T = 200$ nm, $\Delta x_{12} = 40$ nm. The computational procedure is nearly identical to the general computational procedure described in Sec. II, except for the absence of the restoring spring force, which was found to be unnecessary due to the constraints introduced by the periodic boundary condition. The durations of the relaxation/quenching and thermalization at 300-K stages of the sample preparation procedure were both 0.25 ns.

After the sample preparation, a constant heat flux is generated and the total intertube conductance G is evaluated as described in Sec. II. The conductance G differs between simulated configurations due to variations in the area of intertube interaction. Thus the value of the heat flow rate Q_{HB} is varied between 0.6 and 2.4 eV ps^{-1} for different simulations in order to obtain similar values of $\Delta T_{12} \sim 100$ K for all configurations. The average conductance per overlap length σ_T is obtained by dividing G by the total length of both overlap regions.

The second series of simulations is performed for configuration of CNTs illustrated in Fig. 3(b). The computational setup is nearly identical to the one used in the first series of simulations discussed above, with the following exceptions: free boundary conditions are applied in all directions and a restoring spring force is applied individually to each CNT to prevent complete alignment, as described in Sec. II. As no periodic boundary conditions are applied in this series of simulations, no adjustments are made to control pressure. Only one simulation is performed in this series with $L_T = 100$ nm and $\Delta x_{12} = 10$ nm, as a means of comparing the predicted values of σ_T obtained by different methods. The final values of σ_T predicted in both series of simulations are plotted as a function of the overlap length for one contact region Δx_{12} in Fig. 4. Error bars represent the associated variation in the final value, as described in Sec. II.

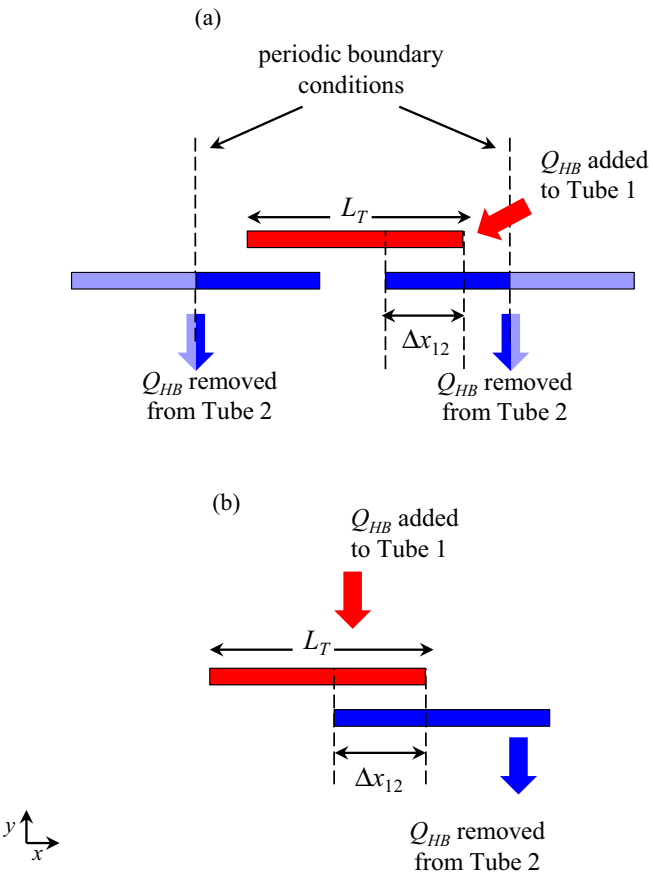

FIG. 3. Schematic representations of the configurations of parallel CNTs employed in simulations performed (a) with periodic boundary conditions in the x direction, CNT length $L_T = 100$ and 200 nm, and two overlap regions of varying overlap length Δx_{12} and (b) with free boundary conditions in all directions, CNT length $L_T = 100$ nm, overlap length $\Delta x_{12} = 10$ nm, and restoring spring forces applied to the entirety of each tube to prevent large-scale translation from the initial positions.

The values of the conductance plotted in Fig. 4 are close to the ones reported earlier by Xu and Buehler [55] and Volkov *et al.* [59] and shown in Fig. 1, with relatively minor quantitative differences related to the differences in the interatomic potentials and shorter length of the CNTs ($L_T = 25$–75 nm) used in Ref. [55]. Similarly, the differences between the moderate decrease in the conductance that extends up to overlap lengths of 40 nm in Fig. 4 and is absent for overlaps exceeding 10 nm in Fig. 1(b) is likely to be related to the difference in the interatomic potentials used in the two studies. The much smaller values of the conductance predicted by Zhong and Lukes [53] [Fig. 1(a)] can be attributed to the effect of the fixed boundary conditions applied at the ends of the interacting CNTs and even shorter length of the CNTs ($L_T = 5$–40 nm) used in this study. The predicted value of σ_T

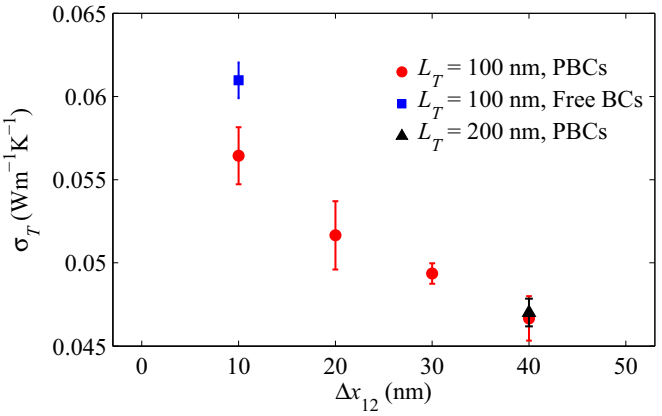

FIG. 4. The results of the calculations of the conductance per overlap length σ_T as a function of the length of one overlap region Δx_{12} obtained for configurations of overlapping CNTs with length $L_T = 100$ nm, overlap length $\Delta x_{12} = 10$, 20, 30, and 40 nm, and periodic boundary conditions as shown in Fig. 3(a) (red circles), length $L_T = 200$ nm, overlap length $\Delta x_{12} = 40$ nm, and periodic boundary conditions (black triangle), and length $L_T = 100$ nm, overlap length $\Delta x_{12} = 10$ nm, and free boundary conditions in all directions as shown in Fig. 3(b) (blue square). The error bars show the uncertainty in the calculated values, as represented by one sample standard deviation of all sequential calculations of G obtained after achievement of a steady state, divided by total overlap length. Predicted values of σ_T decrease with increasing overlap length, which is consistent with the trend observed in previous studies [53,55] and plotted in Fig. 1(a).

for $L_T = 200$ nm and $\Delta x_{12} = 40$ nm is slightly greater than the one for $L_T = 100$ nm and $\Delta x_{12} = 40$ nm, which is consistent with the trend observed in Fig. 1(b). However, in both the present study and the previous study by Volkov *et al.*, the differences in predicted values for σ_T for the two different CNT lengths are not statistically significant, given the measure of uncertainty in the calculations. A more detailed investigation into the effects of CNT length on the conductance across CNT-CNT contacts was performed for a different arrangement of CNTs and is described in Sec. III B.

As shown in Fig. 4, the value of σ_T for $L_T = 100$ nm and $\Delta x_{12} = 10$ nm is about 8% larger for the single-contact configuration, depicted in Fig. 3(b), than for the double-contact configuration depicted in Fig. 3(a). This difference can be attributed to the effect of the boundary conditions (free versus periodic) as well as the possible sensitivity of the intertube conductance to the presence of a neighboring contact. The latter effect is further investigated, albeit for a different contact configuration, in Sec. III C.

B. Effect of CNT length

A series of simulations is performed to resolve the nature and magnitude of the effect CNT length on CNT-CNT conductance. Figure 5 illustrates the arrangement of CNTs in this series of simulations. Two perpendicular (10,10) CNTs of equal length, L_T, are brought in contact to form a cross junction. Tube 1 is orientated along the y axis and tube 2 is orientated along the x axis. Periodic boundary conditions are applied in the x and y directions, and free boundary conditions

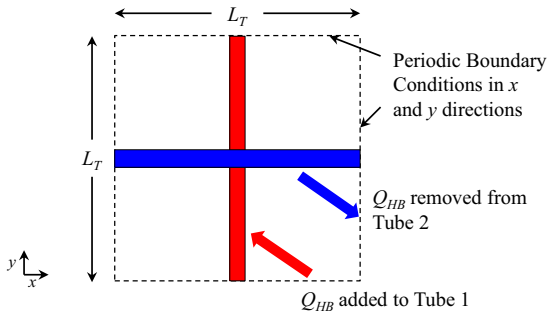

FIG. 5. A schematic of a configuration employed to investigate the effect of CNT length on CNT-CNT conductance. Energy is uniformly added to Tube 1 and uniformly removed from tube 2 at a rate of Q_{HB}. The lengths of both tubes, L_T, are identical and varied between simulations.

are applied in the z direction. Six independent configurations are constructed this way, each with different CNT length L_T ranging from 5 to 200 nm.

The sample preparation routine and computational procedure used for reaching the steady state conditions and calculating the final conductance are described in Sec. II. Each system undergoes a 0.5-ns period of relaxation and 0.5-ns period of gradual heating to 300 K. Energy is added to tube 1 at a rate of 0.16 eV ps^{-1} by scaling the velocities of all atoms in tube 1, while energy is removed from tube 2 at a rate of -0.16 eV ps^{-1} by scaling the velocities of all atoms in tube 2. The final G values are plotted as a function of L_T in Fig. 6, and are represented as red circles with error bars indicating one sample standard deviation of all calculations of G used in determining the final mean value. CNT-CNT conductance

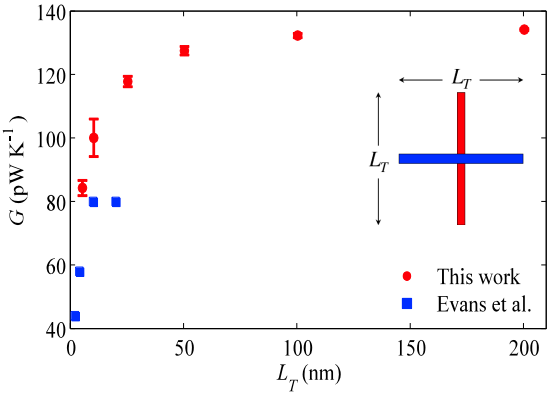

FIG. 6. The values of CNT-CNT conductance G as a function of CNT length L_T calculated in this study (red circles) and reported by Evans *et al.* [58] (blue squares). The error bars show the uncertainty in the values calculated in this work, as represented by one sample standard deviation of all sequential calculations of G obtained after achievement of a steady state. This value can vary between simulations as it is dependent on the statistical noise associated with the calculation of the temperature of each tube and the temperature difference between the tubes ΔT_{12} both of which vary between simulations. The present study and the calculations by Evans *et al.* predict similar values of G for CNT lengths $L_T \leqslant 10$ nm. For longer CNT lengths, Evans *et al.* predict an abrupt deviation from the trend and a lower saturation limit.

is observed to increase with CNT length over the range of lengths studied. The effect is the strongest for shorter CNTs and diminishes as L_T approaches 200 nm.

The results of the simulations reveal a stronger effect over a longer range of CNT lengths as compared to most of the earlier studies. Xu and Buehler [55] concluded that the length effect was small enough to disregard for lengths between 25 and 75 nm. Hu and Cao [69] investigated the thermal resistance at the interface between crossed CNTs with lengths less than 9 nm. Similarly to our observations, their results show a decrease of the thermal resistance with increasing CNT length for shorter CNTs, but suggest saturation of the length dependence near $L_T \approx 9$ nm. Hu and McGaughey [71] studied the effect of CNT length on the conductance between perpendicular CNTs with lengths ranging between 20 and 200 nm. Although a quantitative comparison between their results and the results of the present study is not possible due to differences in the type of the CNTs (smaller diameter (6,6) CNTs are studied in Ref. [71]) and interatomic potential parameters employed [70], the qualitative trends are similar, with a length dependence still observed as L_T approaches 100 nm in both works. Another investigation was performed by Evans *et al.* [58] with a procedure that was almost identical to the one used in the present study. The Tersoff potential was implemented in combination with the LJ potential to describe nonbonded interactions. The authors cite almost the same potential parameters ($\sigma = 3.40$ Å, $\epsilon = 3.0$ meV) as employed in the simulations presented here ($\sigma = 3.41$ Å, $\epsilon = 3.0$ meV). Note that the values of the potential parameters used in the present study and obtained through private communications with Dr. Evans were from another study by the same authors [68] designed to investigate the effect of CNT-CNT contact density on CNT-CNT conductance, which is also investigated in the present work. The potential parameters used in all three of these studies are so close to each other that it is reasonable to quantitatively compare the results of Evans *et al.* [58] and the results obtained in the present study. The blue squares shown in Fig. 6 represent the results reported by Evans *et al.* These results appear to be consistent with the trend seen in the current study for lengths $L_T \leqslant 10$ nm, but show a deviation from this trend for length greater than $L_T = 10$ nm, with G reaching a saturation limit by $L_T = 20$ nm. This inconsistency in results affects the prediction of the maximum conductance and the length at which G can be considered to be nearly independent of CNT length.

This point may be better illustrated by applying the linear extrapolation technique [70,76,77], that enables extrapolation of the predicted values of G beyond the range of CNT lengths in the simulations. The estimates of the thermal conductance between infinitely long CNTs G_∞ can be obtained by plotting the dependence of $1/G$ on $1/L_T$ predicted in NEMD simulations and extrapolating it to $L_T \to \infty$. Figure 7 shows the result of this procedure applied to data obtained in this work and shown in Fig. 6. Extrapolating to $1/L_T = 0$ yields a prediction of $G_\infty = 135$ pW K^{-1}. Evans *et al.* followed the same linear extrapolation procedure for their results and predicted a value of $G_\infty = 91$ pW K^{-1}. For further comparison of the different trends, $L_{0.95}$ can be defined as the CNT length, which corresponds to a predicted conductance $G = 0.95G_\infty$. This provides a quantitative way to compare the point at

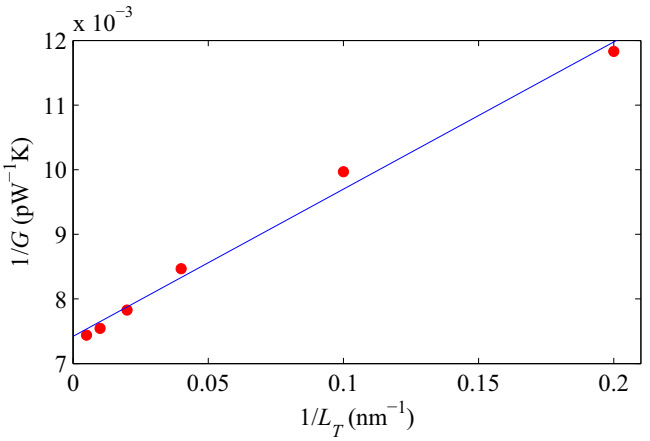

FIG. 7. Inverse of conductance G plotted with respect to the inverse of CNT length L_T. The linear extrapolation is used to predict the conductance between two infinitely long CNTs.

which G has nearly reached the saturation limit and further increase in CNT length does not yield a significant increase in conductance. This length is found to be $L_{0.95} = 59$ nm for the current work and $L_{0.95} = 42$ nm for the data by Evans *et al.*.

Thus the results of the present study suggest a stronger effect of CNT length on CNT-CNT conductance, with 48% higher G_∞ and 40% longer $L_{0.95}$ than predicted in a similar, albeit less extensive, study [58]. These findings have implications for the analysis of thermal transport in CNT-based materials, as well as for interpretation of the results of atomistic studies of intertube conductance.

C. Effect of contact density

A series of simulations is performed to investigate the effect the contact density has on CNT-CNT conductance. One way to quantify the contact density is by the distance between contacts. Figure 8 illustrates the configuration used in this series of simulations. The setup is similar to the configuration employed in Sec. III B, with the addition of a third CNT, Tube 3, which forms a second cross-junction with tube 1. Periodic

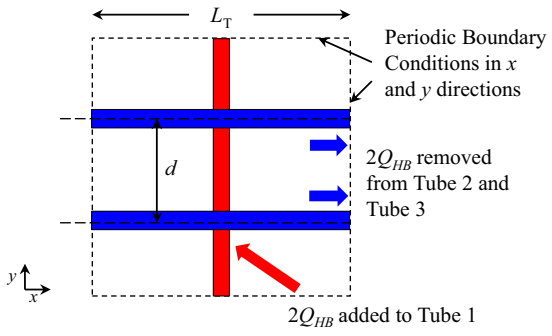

FIG. 8. A schematic of the configuration employed to investigate the effect of contact density on CNT-CNT conductance. Energy is uniformly added to Tube 1 and uniformly removed from tubes 2 and 3 at a rate of $2Q_{\mathrm{HB}}$. The lengths of all tubes L_T is 100 nm and the distance between the centerlines of tube 2 and 3, d, is varied between simulations.

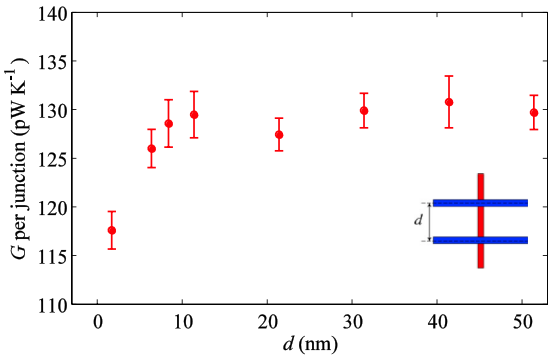

FIG. 9. The conductance G per junction plotted with respect to the distance between junctions d. The error bars show the uncertainty in the calculated values, as represented by one sample standard deviation of all sequential calculations of G obtained after achievement of a steady state. There is no statistically significant effect from the presence of neighboring junctions, except for the case when $d \approx 1.7$ nm, the equilibrium separation distance, which demonstrates a ∼10% reduction.

boundary conditions are applied in the x and y directions and free boundary conditions are applied in z direction. In this series, the lengths of all three CNTs are fixed at 100 nm. The centerlines of tubes 2 and 3 are separated by distance d, which is varied between simulation runs. In this way, the conductance per junction is measured as a function of the junction separation distance.

The sample preparation routine is as described in Sec. II, with each system undergoing a 0.5-ns period of relaxation and 0.5-ns period of gradual heating. After the system has been equilibrated at 300 K, energy is added to tube 1 at a rate of 0.15 eV ps^{-1} in the same manner as described above. Energy is removed from tubes 2 and 3 at the total rate of 0.15 eV ps^{-1}. In this way, an average heat flow rate of $Q_{\mathrm{HB}} = 0.075$ eV ps^{-1} is maintained across each individual junction. The computational procedure to determine steady state and calculate the final conductance is the same as the procedure described in Sec. II with an additional step of dividing the final conductance by 2 to determine the conductance per junction, which is plotted with respect to the junction separation distance in Fig. 9. For all but the lowest separation distance, the restoring spring force described in Sec. II is applied to each tube individually to ensure the average separation distance is maintained throughout the duration of the simulation. The lowest separation distance of $d \approx 1.7$ nm corresponds to the equilibrium separation distance between tubes 2 and 3. In this case, the spring force is applied to both tubes as a whole, keeping the pair centered on tube 1 but not affecting the separation distance between the pair.

The data show no statistically significant effect of the presence of neighboring junctions for distances $d \geqslant 5$ nm. Furthermore, there is only roughly a ∼10% decrease in conductance when the tubes are separated by their equilibrium separation distance, $d \approx 1.7$ nm. With the separation distance d defined as the distance between centerlines of tubes 2 and 3 at the start of the simulation, there are no initial attractive forces between the tubes when the separation distance exceeds the tube diameter plus the 1 nm cutoff distance of the LJ potential describing the van der Waals intertube interactions, i.e., when $d \geqslant 2.4$ nm. In all simulations performed for d between 2.4 and 3 nm, however, the attractive forces between tubes 2 and 3 appear in the course of the simulations due to thermal fluctuations of the shapes of the CNTs and draw the tubes towards each other. The attractive forces are sufficiently strong to overcome the restoring spring forces and to bring the CNTs close to the equilibrium separation from each other. As a result, the values of the conductance calculated in these simulations are all close to the one obtained in the simulation performed for the equilibrium separation distance. Thus the data can be segmented into two distinct cases. In the first case, the initial separation distance is such that there are no direct interactions between tubes 2 and 3 and the conductance per junction is unaffected by the presence of the neighboring junction. In the second case, the initial separation distance is small enough to allow an attractive force between tubes 2 and 3. The two tubes are drawn close to their equilibrium separation distance and conductance per junction decreases by ∼10%.

A somewhat stronger sensitivity to the presence of neighboring CNTs was reported in a similar study by Hu and McGaughey [71] who found a ∼20% reduction in conductance per junction when neighboring junctions were separated by relatively large distances of 10 or 20 nm for CNTs with $L_T = 60$ nm. However, the same study found no significant reduction in conductance for neighboring junctions separated by 10 nm for CNTs with $L_T = 30$ and 90 nm. On the other hand, for small distances between the neighboring junctions, calculations by Prasher *et al.* [51] predict a dramatic reduction of the intertube conductance, with the total conductance of two junctions separated by 0.816 nm being an order of magnitude smaller than that of a single junction. The conclusions of the present study are in a sharp contrast with this earlier prediction and suggest that the intertube contact conductance has very weak sensitivity to the presence of neighboring junctions even at the smallest distances that can be realized in real materials. Given that thermal resistance of CNT-CNT contacts is known to be one of the limiting factors defining the thermal transport in CNT networks [61,62], the findings presented here have important implications for designing CNT-based materials for thermal management applications. Even when the CNTs that make up the adjacent junctions are in direct contact with each other (are separated by the equilibrium distance), the reduction of the contact conductance at each junction is only ∼10%. These findings suggest that overall conductance of a CNT network material can be increased by increasing the number of CNT-CNT contacts.

D. Effect of contact area and the density of interatomic intertube interactions

A series of simulations was performed to investigate the effect of contact area on conductance at the interface between two CNTs forming a junction with angle θ between them. The computational setup used in these simulations is shown in Fig. 10. Adjusting the value of θ results in alterations of the physical configuration of the junction and allows the contact area to be varied from a minimum value at $\theta = 90°$ to a maximum value at $\theta = 0°$. Free boundary conditions are applied in all directions. The two CNTs have the same length

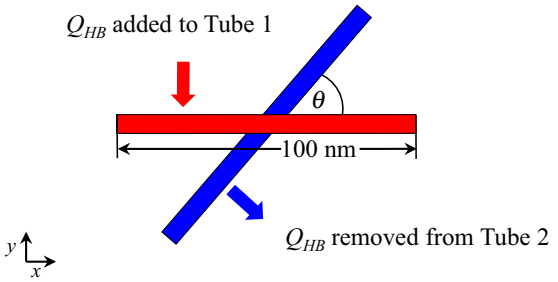

FIG. 10. A schematic of the computational setup employed to investigate the effect of contact area on conductance of a CNT-CNT junction. Energy is uniformly added to tube 1 and uniformly removed from tube 2 at a rate of Q_{HB}. The lengths of both tubes are 100 nm and the angle θ is varied between simulations.

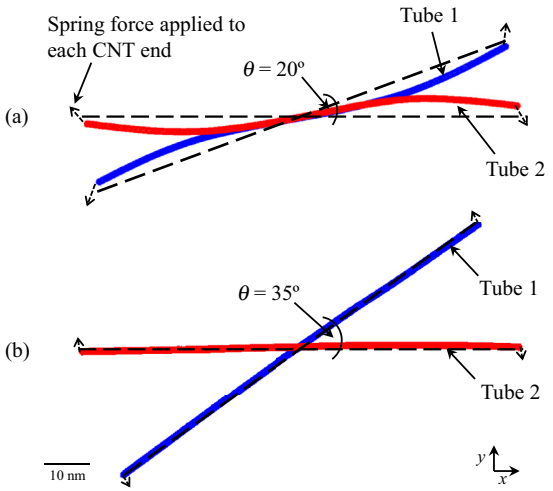

FIG. 11. Representative atomic configurations observed for initial intertube angles of (a) $\theta = 20^{\circ}$ and (b) 35°. A spring force with spring constant $K_{\mathrm{Spr}} = 0.01$ eV Å^{-2} is applied to the 150 atoms in the ends of each CNT to prevent complete alignment of the CNTs. The dashed lines indicate the axes of the original CNT alignment at the start of the simulation. For $\theta = 20^{\circ}$, the central region of each CNT deforms to minimize the intertube interaction energy, thus altering the local configuration at the junction. For all configurations with $\theta \geqslant 35^{\circ}$, the CNT alignment during the constant flux implementation remains nearly identical to the initial alignment.

of 100 nm and are covered by 110-atom caps at the ends, with one of the caps interfacing with the nanotube by a 20-atom ring constituting a half of the nanotubes unit cell.

The preparation of the initial samples follows the general procedure described in Sec. II, with the periods of relaxation and gradual heating to 300 K being 0.25 ns each. In order to prevent spontaneous alignment of CNTs in configurations where initial θ is greater than 0°, small spring forces are applied to the ends of each CNT. The implementation of the spring force is similar to the one described in Sec. II, except that the force is applied only to the 150 atoms at each end of each CNT (110-atom cap and two adjacent 20-atom rings) instead of the even distribution of the force among all atoms in the CNTs used in simulations discussed in Secs. III A–III C. With this approach, the ends of each CNT are tethered to their original positions by spring forces while the central region of each CNT is allowed to bend and distort around the contact area. For consistency, the spring force is applied to the ends of each CNT during the preparation of every configuration, including $\theta = 0^{\circ}$. The value of the spring constant of $K_{\mathrm{Spr}} = 0.0003$ eV Å^{-2} (see discussion in Sec. II) was used in all simulations performed at $\theta > 35^{\circ}$ and $\theta = 0^{\circ}$. In two simulations with low initial values of θ ($\theta = 20^{\circ}$ and 35°), the attractive van der Waals interactions between the nanotubes [78] were able to overcome the original small spring forces and cause almost complete alignment of the CNTs. In order to prevent the alignment and to produce contact configurations that are distinct from the one obtained at $\theta = 0^{\circ}$, the spring constant was increased in these two simulations to $K_{\mathrm{Spr}} = 0.01$ eV Å^{-2}. Snapshots of final atomic configurations, with axes of the original CNT alignments before the relaxation are plotted in Fig. 11. In the simulation with initial $\theta = 20^{\circ}$, shown in Fig. 11(a), the central region of each CNT undergoes substantial deformation to minimize the intertube interaction energy, thus altering the local configuration at the junction. In the case of initial $\theta = 35^{\circ}$, shown in Fig. 11(b), the final configuration is close to the initial one, which is also the case for all other simulations performed with $\theta > 35^{\circ}$ and the original spring constant of $K_{\mathrm{Spr}} = 0.0003$ eV Å^{-2}.

After the sample preparation, a constant heat flux is generated and the total intertube conductance G is calculated as described in Sec. II. The value of the heat flow rate Q_{HB} is varied between 0.08 and 3.0 eV ps^{-1} across this series of simulations in order to obtain similar values of $\Delta T_{12} \sim 100$ K for configurations with different contact conductance. The time required to reach the steady state temperature profile scales with the conductance of the CNT-CNT contact and was within the range of 8 to 30 ns.

The next step in the analysis, defining the area of contact between two cylindrical objects, is nontrivial and a number of alternative definitions have been used in previous studies. In particular, a constant value of the cross-sectional area of a single CNT was used in the calculations of interfacial thermal conductance/resistance between partially overlapping, parallel CNTs in Refs. [53,55], regardless of the overlap length. The question on the definition of the contact area is circumvented in Ref. [59] and Sec. III A by discussing the results in terms of conductance per overlap length (W m^{-1} K^{-1}) that can be assumed to be linearly proportional to the conductance per area for sufficiently long overlaps. For nanotubes crossing each other at an angle θ, a geometrical definition of contact area as $D^2/\sin(\theta)$, where D is the nanotube diameter, was used in Ref. [71]. These simplified approaches cannot be adopted in the present study, where the goal is to formulate a general model of CNT-CNT conductance applicable to junctions of arbitrary configuration, including not only the idealized ones shown in Figs. 3, 5, and 10, but also more complex junctions, e.g., Fig. 11(a), which are, presumably, more representative of intertube contacts present in real CNT materials.

In general, defining a true area of contact on the atomic scale is made difficult by atomic-scale roughness [79,80]. One approach is to consider the number of atoms interacting across the interface [79–83]. For example, Diao *et al.* [83] performed NEMD simulations to investigate the interfacial thermal conductance between a Si surface and both capped

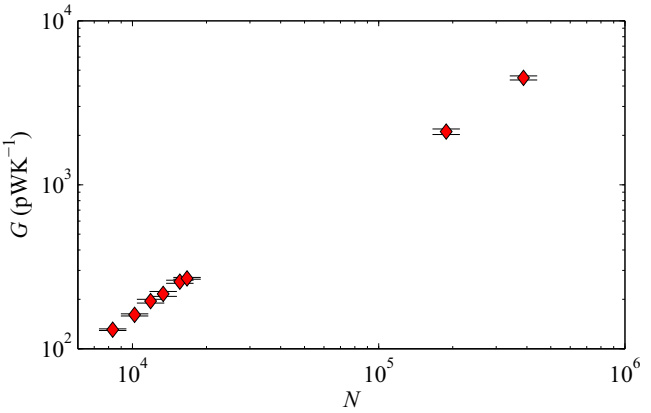

FIG. 12. Predicted values of G plotted with respect to the total number of interatomic interactions between CNTs, N. Error bars represent one sample standard deviation of the sample set of G values calculated in the steady state regime and are provided as a measure of uncertainty. The conductance is observed to increase with increasing N.

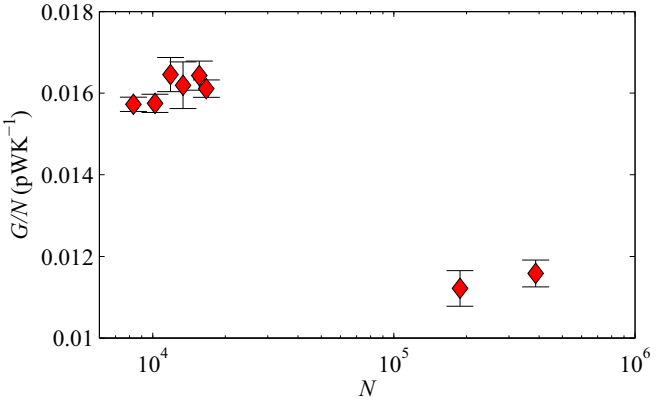

FIG. 13. Values of the average conductance per intertube interaction, G/N, plotted with respect to the total number of interatomic interactions between CNTs, N. The ranges of the error bars are determined by dividing the sample standard deviations of G predictions by the values of N for each configuration and are provided as a measure of uncertainty. The data consist of two distinct groups, with configurations with relatively low values of N (i.e., initial $\theta \geqslant 35^\circ$) having values of G/N, which are all similar to each other and higher than the values of G/N for configurations with higher values of N (i.e., initial $\theta = 20^\circ$ and 0°), which are also similar to each other.

and open-ended CNTs. Their results showed that an increase in interfacial thermal conductance with increasing applied pressure could be explained by an increase in the number of chemical bonds formed between the CNTs and the Si surfaces. Gotsmann and Lantz [79] measured the thermal conductance across the interface between a Si probe tip and a film of tetrahedral amorphous carbon under varied levels of pressure. They constructed a model which showed a good agreement with experimental results by considering additive contributions of atom-atom interactions to the contact conductance between the probe tip and the film.

It is indeed intuitive to consider the effective contact area between CNTs to be related to the number of interatomic intertube interactions as these interactions will be responsible for intertube conductance. The total number of interatomic interactions between CNTs in MD simulations can be determined by counting the total number of pairs of atoms that belong to different CNTs and are within the cutoff distance of the LJ potential describing the van der Waals intertube interactions. The total number of interatomic intertube interactions was evaluated at each time step for which an instantaneous value of G was recorded in the steady state to produce a sample set of 10 values. The total number of interatomic interactions between CNTs, N, is taken as the mean of this sample set and is used to characterize the contact region for each simulation configuration. The final value of G is plotted with respect to the total number of interatomic interactions for each simulation in Fig. 12.

As can be seen in Fig. 12, the predicted values of conductance G increase with increasing number of interatomic interactions, N. This trend is reasonable considering that N characterizes the level of interaction responsible for thermal conductance. Despite the apparent trend in Fig. 12, the values of the conductance are not uniquely defined by the number of interatomic intertube interactions. This can be illustrated by considering the conductance *per interaction* shown in Fig. 13. The values of G and standard deviation indicated by the error bars in Fig. 12 are divided by N to characterize the average conductance per interatomic interaction. Results fall into two distinct groupings where configurations with initial $\theta \geqslant 35^\circ$ have a total number of interactions ranging from $\sim 8.3\times10^3$ to $\sim 1.7\times10^4$ and configurations with initial $\theta = 20^\circ$ and $\theta = 0^\circ$ have $\sim 1.9\times10^5$ and $\sim 3.9\times10^5$ interactions, respectively. Moreover, all values of G/N for the group of configurations with lower N are similar to each other and greater than the values of G/N for the group of configurations with greater N, which are also close to each other.

The nature of the variation of G/N suggests that there is a distinct difference between the two groups of configurations. The earlier observation that the conductance per unit overlap length σ_T between partially overlapping parallel CNTs does not depend on the overlap length for long, 10s of nm, overlaps [59] but exhibits a strong length dependence for short overlaps [53,55] (see Fig. 1) indicates that the distinct difference between values of G/N for the two groups of configurations is not simply due to variation in contact area or N alone. There appears to be a characteristic difference between the two groupings that is not fully captured by N. Further investigation into the geometry of the contact regions reveals another distinct difference between the two groups of configurations. Namely, the average number of intertube interactions per atom in the contact region, M, is found to be different for each group of configurations. This value, defined as twice the total number of van der Waals interatomic intertube interactions divided by the total number of atoms involved in intertube interactions, provides a measure of the average number of interatomic intertube interactions experienced by each atom in the intertube interaction region.

Similar to the calculation procedure for N, sample calculations of M are taken for each timestep for which an instantaneous value of G was recorded and the final value of M is taken as the mean of this sample set. The values of

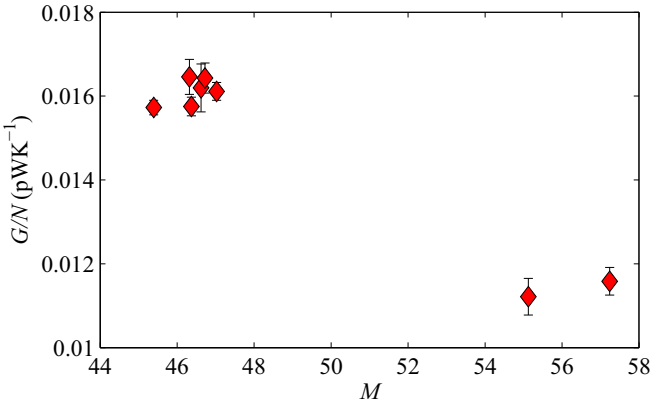

FIG. 14. Predicted values of the average conductance per intertube interaction, G/N, plotted with respect to the average number of intertube interactions per atom in the contact region, M. The ranges of the error bars are determined by dividing the sample standard deviations of G values by the values of N for each configuration and are provided as a measure of uncertainty. The data form two distinct groups, with configurations with initial $\theta \geqslant 35^\circ$ having relatively lower values of M due to a greater proportion of atoms in the contact regions being located in the periphery of the contact. Greater predicted values of G/N are observed for configurations with relatively lower values of M, suggesting that the conductance per interaction is greater in areas with smaller density of intertube interactions.

G/N are plotted with respect to M for each configuration in Fig. 14. Just as in Fig. 13, the data splits into two groups. The values of M for configurations with initial $\theta \geqslant 35^\circ$ fall within a range from 45.4 to 47.0, while configurations with initial $\theta = 20^\circ$ and $\theta = 0^\circ$ have values of $M = 55.1$ and 57.2, respectively. It is not surprising that configurations with higher initial values of θ have a lower average number of interatomic intertube interactions per atom in the contact region as compared to configurations with lower initial values of θ. Atoms located at the periphery of a contact region have less intertube interactions than atoms located in the central part of a contact region and the geometries of the configurations with high initial values of θ are such that the periphery accounts for a higher fraction of the overall contact regions. As a result, these configurations have smaller average numbers of intertube interactions per atom.

The configurations that belong to the group with lower values of M are observed to have higher values of G/N as compared to ones with higher values of M. This observation suggests that contributions of local areas of a contact (or corresponding atoms) to the total contact conductance are greater at the periphery of the contact, where each atom participates in a smaller number of interatomic intertube interactions. While the computational prediction of the enhanced contribution to the contact conductance from areas of the CNTs that are more distant from the neighboring tubes and have smaller intertube interaction energy density may appear counterintuitive from first glance, it is actually consistent with the results of the studies by Zhong and Lukes [53] and Xu and Buehler [55] discussed in Sec. I. The conductance per overlap length between parallel partially overlapping CNTs, calculated from data obtained in these studies and shown in Fig. 1(a), is greater for small overlap lengths which correspond to contact areas where the lower interaction energy density regions account for a higher fraction of the overall contact area. The summation of these results and the results presented in this section suggests that any predictive model of conductance at CNT-CNT contacts of arbitrary configuration should account for the dependence on both the area of the contact region, which can be quantified by N, and the density of interatomic intertube interactions in the contact region, which can be characterized by M.

IV. GENERAL DESCRIPTION OF CNT-CNT CONDUCTANCE

The results of the MD simulations discussed in Sec. III for different types of CNT-CNT contacts can now be used to design and parametrize a general predictive model of intertube conductance that would be applicable to an arbitrary configuration of the CNTs. The heterogeneity of the local environment throughout the contact between two adjacent, cylindrical CNTs prevents us from applying simple and uniform descriptions of the contacts in terms of the overlap area/length [59], contact angle [71], or total intertube binding energy [58]. Rather, following the conclusions of the analysis presented in Sec. III D, the intertube contacts will be characterized by the number of interatomic interactions between the CNTs and the density of interatomic intertube interactions in the contact region.

It is well established that thermal conductance across a material interface decreases with decreasing strength of interatomic interactions across the interface [84–87]. Thus, when characterizing the contact region in terms of the total number of interatomic intertube interactions, it is reasonable to scale the contributions of atomic pairs by a scaling factor that accounts for diminishing contributions to the contact conductance from weak interatomic interactions at the tail the LJ potential describing the van der Waals intertube interactions. One natural choice of the scaling factor is to use the LJ interatomic potential function itself, so that the contribution from a pair of atoms i and j that belong to different tubes and are separated by distance r_{ij} is

$$n(r_{ij}) = \begin{cases} 1, & r_{ij} < r_m \\ 2\left(\frac{r_m}{r_{ij}}\right)^6 - \left(\frac{r_m}{r_{ij}}\right)^{12}, & r_m \leqslant r_{ij} \leqslant r_c \\ 0, & r_{ij} > r_c \end{cases}, \tag{2}$$

where r_c is the cutoff distance of the potential, $r_m = 2^{1/6}\sigma$ is the separation distance that corresponds to the minimum of the potential, and σ is the length parameter of the LJ potential. With this scaling factor, each atomic pair with a separation distances of $r_{ij} < r_m$ is counted as one interaction, whereas the contributions from pairs with $r_m \leqslant r_{ij} \leqslant r_c$ are scaled by the absolute value of the LJ potential normalized to unity at $r_{ij} = r_m$, as shown in Fig. 15. In this formulation, the total "effective" number of interatomic intertube interactions N_{eff} is

$$N_{\text{eff}} = \sum_i \sum_j n(r_{ij}), \tag{3}$$

where index i is varied over the indices of all atoms in one CNT and index j is varied over the indices of all atoms in the neighboring CNT. The value of N_{eff} provides a quantitative

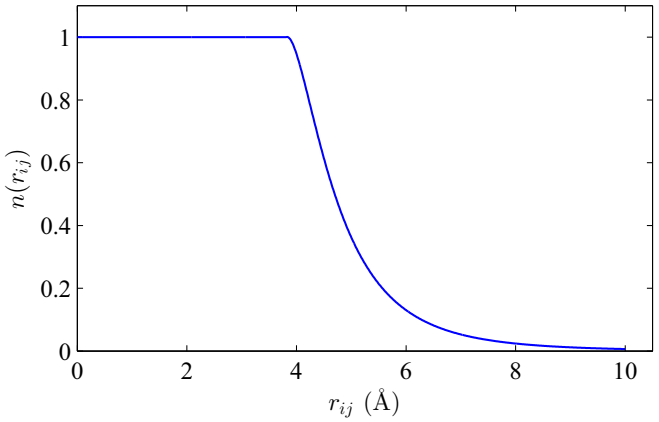

FIG. 15. The scaling factor n, described by Eq. (2) and defining the contribution of each intertube atomic pair to the total "effective" number of interatomic intertube interactions, N_{eff}, based on the separation distance between the atoms, r_{ij}.

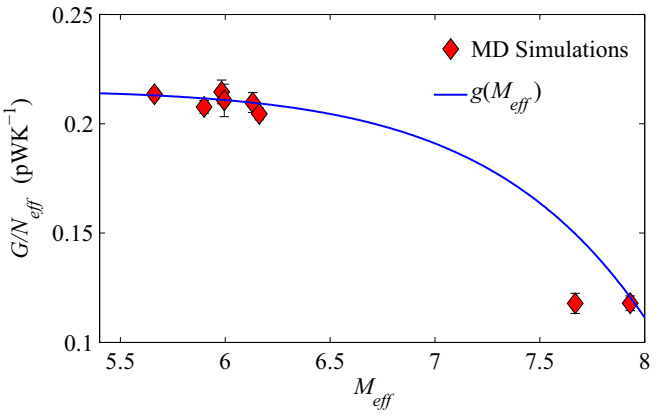

FIG. 16. The conductance per total "effective" number of interatomic intertube interactions, G/N_{eff}, plotted as a function of the average number of "effective" interatomic intertube interactions per atom in the contact region, M_{eff}. Values of G/N_{eff} are calculated in MD simulations described in Sec. III D and are represented by red circles. The error bars represent the standard deviations of the instantaneous values of G divided by the mean values of N_{eff}. The blue curve represents function $g(M_{\text{eff}})$, defined by Eq. (4) and fitted to the results of the MD simulations. The value of G/N_{eff} at $M_{\text{eff}} = 7.67$ is not used in the fitting procedure, as explained in the text.

description of the contact region and accounts for nonuniformity of the contact structure by considering the separation distance between each interatomic intertube interaction. Analogous to the definition of M provided in Sec. III D, M_{eff} is defined as the average number of "effective" interatomic intertube interactions per atom in the contact region, i.e., $2N_{\text{eff}}$ divided by the total number of atoms involved in intertube interactions.

The results presented in Sec. III D show that the conductance per interatomic intertube interaction, G/N, exhibits a pronounced dependence on M. This observation suggests that it may be possible to express the total conductance across a CNT-CNT junction as a function of N_{eff} and M_{eff}, such that $G(N_{\text{eff}}, M_{\text{eff}}) = g(M_{\text{eff}}) \cdot N_{\text{eff}}$ where $g(M_{\text{eff}})$ describes the dependence of G/N_{eff} on M_{eff}. Below we test this hypothesis by first finding an expression $g(M_{\text{eff}})$ that would provide a good fit to the conductivity values predicted in MD simulations of CNT cross junctions discussed in Sec. III D and then verifying the expression against additional simulations that were not used in the fitting procedure.

For each simulation discussed in Sec. III D, instantaneous values of N_{eff} and M_{eff} were calculated at each time step for which an instantaneous value of G was recorded in the steady state. The final values of N_{eff} and M_{eff} are taken as the means of the corresponding sample sets of ten calculations. The final values of G are divided by their corresponding values of N_{eff} and plotted with respect to M_{eff} in Fig. 16. The functional form of $g(M_{\text{eff}})$ is taken as

$$g(M_{\text{eff}}) = AM_{\text{eff}}^{B} + C, \tag{4}$$

with parameters $A = -1.62\times10^{-11}$ pW K^{-1}, $B = 10.86$, and $C = 0.2154$ pW K^{-1} determined by fitting Eq. (4) to the data points shown in Fig. 16.

One data point, at $M_{\text{eff}} = 7.67$, cannot be accurately fitted to the empirical expression and was excluded from the fitting procedure. This point corresponds to the MD simulation performed for an initial angle of $\theta = 20^{\circ}$ between the two CNTs. The low value of θ allows for a stronger intertube interaction than in any other configuration of nonparallel CNTs. As the CNTs deform to seek a low-energy configuration, the ends of each CNT are displaced from their original positions, causing the magnitude of the spring force applied to the ends (see Sec. II) to increase. The final configuration, shown in Fig. 11(a), is defined by the balance between the intertube interaction forces and the internal stresses supported by the external spring forces. The results of earlier MD simulations [88,89] have revealed a substantial decrease of the intrinsic thermal conductivity of CNTs experiencing axial, bending, or radial deformation. These results imply a modification of the vibrational spectra of deformed CNTs, which is likely to affect the intertube conductance as well. Moreover, the increased magnitude of the spring force in the distorted configuration may constrain the low-frequency vibrational motions of the CNTs, with the corresponding negative impact on the intertube conductance that is largely defined by the low-frequency vibrational modes. The combined effect of the factors discussed above is likely to be responsible for the overestimation of the conductance determined in this MD simulation by the empirical relation that is not aimed at capturing the effect of internal stresses on the intertube thermal conductance.

With $g(M_{\text{eff}})$ defined, a general predictive model of the conductance at CNT-CNT contacts can be expressed in terms of N_{eff} and M_{eff} as

$$G(N_{\text{eff}}, M_{\text{eff}}) = \left(AM_{\text{eff}}^{B} + C\right)N_{\text{eff}}, \tag{5}$$

where N_{eff} and M_{eff} are determined directly from the atomic coordinates of any arbitrary configuration. The accuracy of this predictive model can now be verified by comparing the values of the CNT-CNT conductance predicted by Eq. (5) and obtained in MD simulations of CNT-CNT contacts that were not used in fitting the equation. These additional simulations include the ones presented in Sec. III A (additional analysis of the computational results was performed to obtain the values

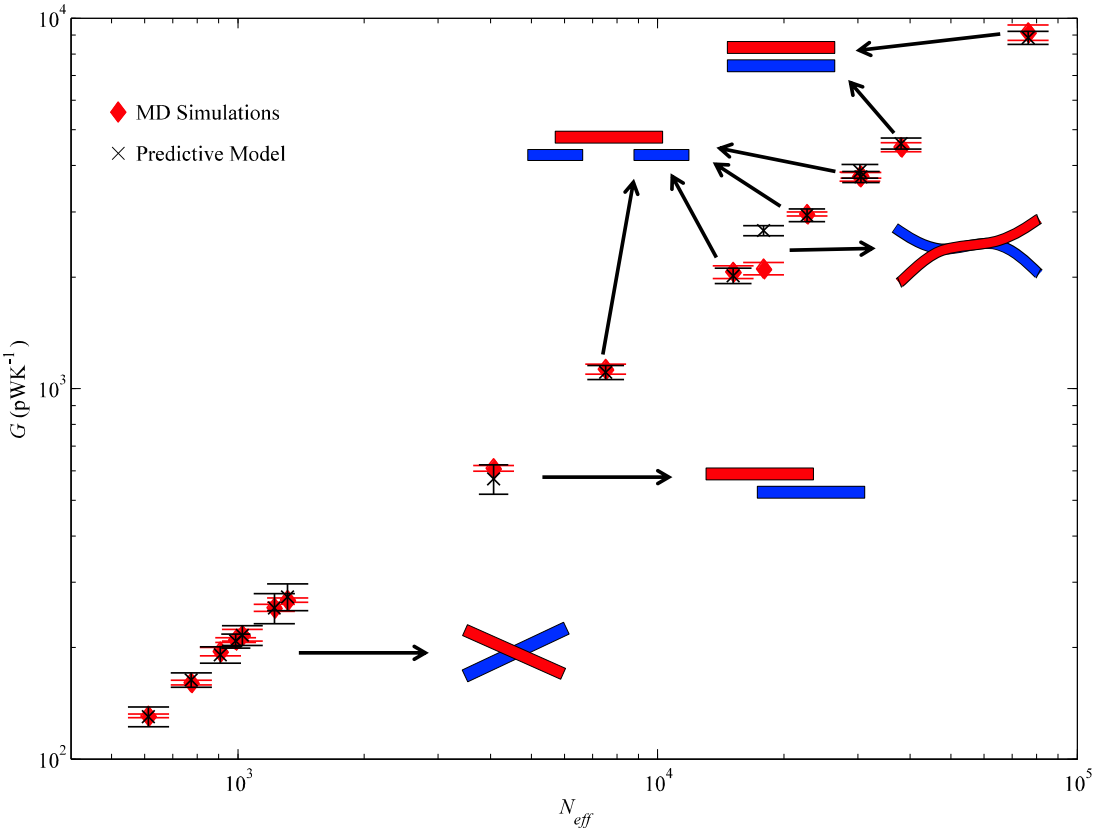

FIG. 17. The values of conductance, G, obtained in MD simulations (red circles) and predicted by Eq. (5) (black crosses), plotted with respect to the total "effective" number of interatomic intertube interactions, N_{eff}. The calculations are performed for a diverse range of contact configurations schematically represented in the figure. Error bars represent one sample standard deviation of the sample sets of values of G calculated by the MD method and the empirical equation.

of N_{eff} and M_{eff} for each of these simulations), as well as two new simulations performed with the computational procedure described in Sec. III D for CNTs with of length $L_T = 200$ nm and initial angles $\theta = 0^\circ$ and 45°.

The results of all calculations performed in this study and discussed above are summarized in Fig. 17. The values of G obtained in MD simulations are shown by red circles, with error bars representing one sample standard deviations of sample sets recorded in the steady state parts of the MD simulations. Similarly, the predictions of Eq. (5) are shown by black crosses with error bars representing one sample standard deviation of the values obtained with Eq. (5) for N_{eff} and M_{eff} evaluated from atomic coordinates recorded during the steady state parts of the corresponding MD simulations. With an exception of one simulation of cross contact with initial $\theta = 20^\circ$ discussed above, all the predictions of Eq. (5) agree with the results of the MD simulations within the statistical error. This is a remarkable observation as a broad variety of dissimilar contact configurations (fully and partially overlapping parallel nanotubes, CNTs crossing each other at different angles) is considered in the simulations and the range of the corresponding values of G spans almost two orders of magnitude. The consistently good description of the thermal conductance of a broad range of diverse contact configurations is achieved by properly accounting for the sensitivity of the conductance to the density of interatomic intertube interactions.

While the functional form of the dependence of the intertube conductance on the parameters of a contact configuration given by Eq. (5) is likely to be applicable to other CNT systems, beyond the (10,10) CNTs used as a model system in this study, the values of parameters A, B, and C in Eq. (5) have to be adjusted for CNTs of different type or different interatomic force fields used in the simulations. Moreover, the CNT length may also affect the parameters of the empirical equation for short CNTs, as the predicted values of G are shown to increase with length for nanotubes shorter than 100 nm in Sec. III B. Finally, a pressure applied to a CNT-CNT junction may have a substantial effect on intertube conductance, as have been demonstrated in calculations reported by Evans *et al.* [58]. While both an increase in contact area and modification of the density of interatomic intertube interactions resulting from deformation of CNTs under applied pressure would naturally change the parameters of Eq. (5), the results of the calculations for a junction with initial $\theta = 20^\circ$ discussed above suggest that the empirical equation is less accurate for systems under significant level of stress.

V. SUMMARY

The results of a systematic NEMD study of the dependence of the intertube conductance on geometrical parameters of CNT-CNT contacts and local environment have revealed the key factors that control the heat exchange between

nanotubes in CNT network materials. Simulations performed for nanotubes of different length demonstrate stronger length dependence present over a broader range of CNT lengths than has been previously reported. The results of these simulations were used in the analysis of heat exchange at CNT contacts, where the range of CNT lengths ($\geqslant$100 nm) was chosen to minimize the effect of CNT length on the intertube conductance. The conductance across CNT-CNT junctions is also shown to be unaffected by the presence of neighboring junctions when the CNTs creating the junctions are outside the range of direct van der Waals interaction with each other. When junctions are separated by the equilibrium separation distance of the two neighboring tubes, the conductance per junction is reduced by only $\sim$10% with respect to an isolated CNT-CNT contact. These results are in a sharp contrast with a previous computational study [51], which predicted an order of magnitude reduction of the contact conductance in a double junction, and have important implications for interpretation of experimental measurements of the effective conductance of CNT materials.

The combined results of several series of simulations performed for a diverse range of intertube contact configurations (parallel fully or partially overlapping CNTs and CNTs crossing each other at different angles) reveal a nonlinear dependence of the conductance on the number of interatomic intertube interactions (used as proxy for contact area) and suggest a larger contribution to the conductance from areas of the contact where the density of interatomic intertube interactions is smaller. An empirical relation expressing the conductance of an arbitrary contact configuration through the area of the contact region, quantified by the number of interatomic intertube interactions, and the density of interatomic intertube interactions, characterized by the average number of interatomic intertube interactions per atom in the contact region, is suggested based on the results of NEMD simulations. The empirical relation is found to provide a good quantitative description of the contact conductance for various CNT configurations investigated in the present study. Moreover, the empirical relation and the underlying concept of the sensitivity of the conductance to the density of interatomic intertube interactions reconcile the results of earlier studies of the conductance between parallel partially overlapping CNT, where the conductance per overlap length was shown to be independent of the overlap length for long overlaps [59] but was found to exhibit a pronounced decrease with increasing length of the overlap for short overlaps [53,55].

Overall, the connections between the local structure of CNT contacts and intertube conductance established in this work may provide guidance for the design of CNT materials with thermal transport properties tailored for particular practical applications. The general description of the conductance of an arbitrary CNT-CNT contact configuration is suitable for incorporation into a mesoscopic model capable of dynamic simulations of CNT networks consisting of tens of thousands of interacting nanotubes [59–62,78,90,91] thus enabling analysis of the key microstructural features and elementary processes that control the effective/macroscopic thermal transport properties of CNT materials.

ACKNOWLEDGMENTS

The authors acknowledge financial support provided by the National Aeronautics and Space Administration (NASA) through an Early Stage Innovations grant from NASA's Space Technology Research Grants Program (NNX16AD99G) and by the Air Force Office of Scientific Research (AFOSR) through the AFOSR's Thermal Sciences program (FA9550-10-10545). Computational support is provided by the National Science Foundation (NSF) through the Extreme Science and Engineering Discovery Environment (CTS160026).

[1] V. Datsyuk, I. Firkowska, K. Gharagozloo-Hubmann, M. Lisunova, A. Vogt, A. Boden, M. Kasimir, S. Trotsenko, G. Czempiel, and S. Reich, Carbon nanotubes based engineering materials for thermal management applications, in *27th Annual Semiconductor Thermal Measurement and Management Symposium (SEMI-THERM)* (IEEE, San Jose, CA, 2011), p. 325.

[2] C. Yu, L. Shi, Z. Yao, D. Li, and A. Majumdar, Thermal conductance and thermopower of an individual single-wall carbon nanotube, Nano Lett. **5**, 1842 (2005).

[3] M. Fujii, X. Zhang, H. Xie, H. Ago, K. Takahashi, T. Ikuta, H. Abe, and T. Shimizu, Measuring the Thermal Conductivity of a Single Carbon Nanotube, Phys. Rev. Lett. **95**, 065502 (2005).

[4] H.-Y. Chiu, V. V. Deshpande, H. W. C. Postma, C. N. Lau, C. Miko, L. Forro, and M. Bockrath, Ballistic Phonon Thermal Transport in Multiwalled Carbon Nanotubes, Phys. Rev. Lett. **95**, 226101 (2005).

[5] E. Pop, D. Mann, Q. Wang, K. Goodson, and H. Dai, Thermal conductance of an individual single-wall carbon nanotube above room temperature, Nano Lett. **6**, 96 (2006).

[6] S. Wang, Z. Liang, B. Wang, and C. Zhang, High-strength and multifunctional macroscopic fabric of single-walled carbon nanotubes, Adv. Mater. **19**, 1257 (2007).

[7] I.-K. Hsu, R. Kumar, A. Bushmaker, S. B. Cronin, M. T. Pettes, L. Shi, T. Brintlinger, M. S. Fuhrer, and J. Cumings, Optical measurement of thermal transport in suspended carbon nanotubes, Appl. Phys. Lett. **92**, 063119 (2008).

[8] M. T. Pettes and L. Shi, Thermal and structural characterizations of individual single-, double-, and multi-walled carbon nanotubes, Adv. Funct. Mater. **19**, 3918 (2009).

[9] Q. Li, C. Liu, X. Wang, and S. Fan, Measuring the thermal conductivity of individual carbon nanotubes by the Raman shift method, Nanotechnology **20**, 145702 (2009).

[10] S. Berber, Y.-K. Kwon, and D. Tomanek, Unusually High Thermal Conductivity of Carbon Nanotubes, Phys. Rev. Lett. **84**, 4613 (2000).

[11] J. Che, T. Cagin, and W. A. Goddard III, Thermal conductivity of carbon nanotubes, Nanotechnology **11**, 65 (2000).

[12] M. A. Osman and D. Srivastava, Temperature dependence of the thermal conductivity of single-wall carbon nanotubes, Nanotechnology **12**, 21 (2001).

[13] S. Maruyama, A molecular dynamics simulation of heat conduction in finite length SWNTs, Physica B **323**, 193 (2002).
[14] S. Maruyama, A molecular dynamics simulation of heat conduction of a finite length single-walled carbon nanotube, Microscale Thermophys. Eng. **7**, 41 (2003).
[15] C. W. Padgett and D. W. Brenner, Influence of chemisorption on the thermal conductivity of single-wall carbon nanotubes, Nano Lett. **4**, 1051 (2004).
[16] J. F. Moreland, J. B. Freund, and G. Chen, The disparate thermal conductivity of carbon nanotubes and diamond nanowires studied by atomistic simulation, Microscale Thermophys. Eng. **8**, 61 (2004).
[17] M. Grujicic, G. Cao, and B. Gersten, Atomic-scale computations of the lattice contribution to thermal conductivity of single-walled carbon nanotubes, Mater. Sci. Eng. B **107**, 204 (2004).
[18] M. Grujicic, G. Cao, and W. N. Roy, Computational analysis of the lattice contribution to thermal conductivity of single-walled carbon nanotubes, J. Mater. Sci. **40**, 1943 (2005).
[19] G. Zhang and B. Li, Thermal conductivity of nanotubes revisited: Effects of chirality, isotope impurity, tube length, and temperature, J. Chem. Phys. **123**, 114714 (2005).
[20] K. Zhang, H. Fan, and M. M. F. Yuen, Molecular dynamics study on thermal performance of CNT-array-thermal interface material, in *International Symposium on Electronic Materials and Packaging* (IEEE, Kowloon, China, 2006), p. 1.
[21] K. Bi, Y. Chen, J. Yang, Y. Wang, and M. Chen, Molecular dynamics simulation of thermal conductivity of single-wall carbon nanotubes, Phys. Lett. A **350**, 150 (2006).
[22] J. R. Lukes and H. Zhong, Thermal conductivity of individual single-wall carbon nanotubes, J. Heat Transfer **129**, 705 (2007).
[23] R.-Q. Pan, Z.-J. Xu, and Z.-Y. Zhu, Length dependence of thermal conductivity of single-walled carbon nanotubes, Chin. Phys. Lett. **24**, 1321 (2007).
[24] J. Shiomi and S. Maruyama, Molecular dynamics of diffusive-ballistic heat conduction in single-walled carbon nanotubes, Jpn. J. Appl. Phys. **47**, 2005 (2008).
[25] M. Alaghemandi, E. Algaer, M. C. Bohm, and F. Muller-Plathe, The thermal conductivity and thermal rectification of carbon nanotubes studied using reverse non-equilibrium molecular dynamics simulations, Nanotechnology **20**, 115704 (2009).
[26] C. Ren, W. Zhang, Z. Xu, Z. Zhu, and P. Huai, Thermal conductivity of single-walled carbon nanotubes under axial stress, J. Phys. Chem. C **114**, 5786 (2010).
[27] J. A. Thomas, R. M. Iutzi, and A. J. H. McGaughey, Thermal conductivity and phonon transport in empty and water-filled carbon nanotubes, Phys. Rev. B **81**, 045413 (2010).
[28] B. Qiu, Y. Wang, Q. Zhao, and X. Ruan, The effects of diameter and chirality on the thermal transport in free-standing and supported carbon-nanotubes, Appl. Phys. Lett. **100**, 233105 (2012).
[29] A. Cao and J. Qu, Size dependent thermal conductivity of single-walled carbon nanotubes, J. Appl. Phys. **112**, 013503 (2012).
[30] A. N. Imtani, Thermal conductivity for single-walled carbon nanotubes from Einstein relation in molecular dynamics, J. Phys. Chem. Solids **74**, 1599 (2013).
[31] K. Kordas, G. Toth, P. Moilanen, M. Kumpumaki, J. Vahakangas, A. Uusimaki, R. Vajtai, and P. M. Ajayan, Chip cooling with integrated carbon nanotube microfin architectures, Appl. Phys. Lett. **90**, 123105 (2007).
[32] T. Iwai and Y. Awano, Carbon nanotube bumps for thermal and electric conduction in transistor, FUJITSU Sci. Tech. J. **43**, 508 (2007).
[33] Y. Xu, C.-K. Leong, and D. D. L. Chung, Carbon nanotube thermal pastes for improving thermal contacts, J. Electron. Mater. **36**, 1181 (2007).
[34] H. Huang, C. H. Liu, Y. Wu, and S. Fan, Aligned carbon nanotube composite films for thermal management, Adv. Mater. **17**, 1652 (2005).
[35] Y. Wu, C. H. Liu, H. Huang, and S. S. Fan, Effects of surface metal layer on the thermal contact resistance of carbon nanotube arrays, Appl. Phys. Lett. **87**, 213108 (2005).
[36] T. Tong, Y. Zhao, L. Delzeit, A. Kashani, M. Meyyappan, and A. Majumdar, Dense vertically aligned multiwalled carbon nanotube arrays as thermal interface materials, IEEE Trans. Compon. Packag. Technol. **30**, 92 (2007).
[37] X. Liu, Y. Zhang, A. M. Cassell, and B. A. Cruden, Implications of catalyst control for carbon nanotube based thermal interface materials, J. Appl. Phys. **104**, 084310 (2008).
[38] A. A. Balandin, Thermal properties of graphene and nanostructured carbon materials, Nat. Mater. **10**, 569 (2011).
[39] R. Prasher, Thermal interface materials: Historical perspective, status, and future directions, Proc. IEEE **94**, 1571 (2006).
[40] K. Zhang, M. Yuen, N. Wang, J. Y. Miao, D. Xiao, and H. B. Fan, Thermal interface material with aligned CNT and its application in HB-LED packaging, in *2006 IEEE Electronic Components and Technology Conference* (IEEE, San Diego, CA, 2006), p. 177.
[41] H. Chen, M. Chen, J. Di, G. Xu, H. Li, and Q. Li, Architecting three-dimensional networks in carbon nanotube buckypapers for thermal interface materials, J. Phys. Chem. C **116**, 3903 (2012).
[42] S. Kaur, N. Raravikar, B. A. Helms, R. Prasher, and D. F. Ogletree, Enhanced thermal transport at covalently functionalized carbon nanotube array interfaces, Nat. Commun. **5**, 3082 (2014).
[43] E. Leveugle, L. Divay, H. Le Khanh, J. Daon, E. Chastaing, P. Le Barny, and A. Ziaei, Free standing thermal interface material based on vertical arrays composites, in *19th International Workshop on Thermal Investigations of ICs and Systems* (IEEE, Berlin, Germany, 2013), p. 244.
[44] J. Hone, M. C. Llaguno, N. M. Nemes, A. T. Johnson, J. E. Fischer, D. A. Walters, M. J. Casavant, J. Schmidt, and R. E. Smalley, Electrical and thermal transport properties of magnetically aligned single wall carbon nanotube films, Appl. Phys. Lett. **77**, 666 (2000).
[45] J. Hone, M. C. Llaguno, M. J. Biercuk, A. T. Johnson, B. Batlogg, Z. Benes, and J. E. Fischer, Thermal properties of carbon nanotubes and nanotube-based materials, Appl. Phys. A **74**, 339 (2002).
[46] S. Sinha, S. Barjami, G. Iannacchione, A. Schwab, and G. Muench, Off-axis thermal properties of carbon nanotube films, J. Nanopart. Res. **7**, 651 (2005).
[47] Y. Yamada, T. Nishiyama, T. Yasuhara, and K. Takahashi, Thermal boundary conductance between multi-walled carbon nanotubes, J. Them. Sci. Technol. **7**, 190 (2012).
[48] M. E. Itkis, F. Borondics, A. Yu, and R. C. Haddon, Thermal conductivity measurements of semitransparent single-walled carbon nanotube films by a bolometric technique, Nano Lett. **7**, 900 (2007).

[49] I. Ivanov, A. Puretzky, G. Eres, H. Wang, Z. Pan, H. Cui, R. Jin, J. Howe, and D. B. Geohegan, Fast and highly anisotropic thermal transport through vertically aligned carbon nanotube arrays, Appl. Phys. Lett. **89**, 223110 (2006).

[50] P. Gonnet, Z. Liang, E. S. Choi, R. S. Kadambala, C. Zhang, J. S. Brooks, B. Wang, and L. Kramer, Thermal conductivity of magnetically aligned carbon nanotube buckypapers and nanocomposites, Curr. Appl. Phys. **6**, 119 (2006).

[51] R. S. Prasher, X. J. Hu, Y. Chalopin, N. Mingo, K. Lofgreen, S. Volz, F. Cleri, and P. Keblinski, Turning Carbon Nanotubes from Exceptional Heat Conductors into Insulators, Phys. Rev. Lett. **102**, 105901 (2009).

[52] J. Yang, S. Waltermire, Y. Chen, A. A. Zinn, T. T. Xu, and D. Li, Contact thermal resistance between individual multiwall carbon nanotubes, Appl. Phys. Lett. **96**, 023109 (2010).

[53] H. L. Zhong and J. R. Lukes, Interfacial thermal resistance between carbon nanotubes: Molecular dynamics simulations and analytical thermal modeling, Phys. Rev. B **74**, 125403 (2006).

[54] S. Maruyama, Y. Igarashi, Y. Taniguchi, and J. Shiomi, Anisotropic heat transfer of single-walled carbon nanotubes, J. Them. Sci. Technol. **1**, 138 (2006).

[55] Z. Xu and M. J. Buehler, Nanoengineering heat transfer performance at carbon nanotube interfaces, ACS Nano **3**, 2767 (2009).

[56] V. Varshney, S. S. Patnaik, A. K. Roy, and B. L. Farmer, Modeling of thermal conductance at transverse cnt-cnt interfaces, J. Phys. Chem. C **114**, 16223 (2010).

[57] Y. Chalopin, S. Volz, and N. Mingo, Upper bound to the thermal conductivity of carbon nanotube pellets, J. Appl. Phys. **105**, 084301 (2009).

[58] W. J. Evans, M. Shen, and P. Keblinski, Inter-tube thermal conductance in carbon nanotubes arrays and bundles: Effects of contact area and pressure, Appl. Phys. Lett. **100**, 261908 (2012).

[59] A. N. Volkov, R. N. Salaway, and L. V. Zhigilei, Atomistic simulations, mesoscopic modeling, and theoretical analysis of thermal conductivity of bundles composed of carbon nanotubes, J. Appl. Phys. **114**, 104301 (2013).

[60] A. N. Volkov and L. V. Zhigilei, Scaling Laws and Mesoscopic Modeling of Thermal Conductivity in Carbon Nanotube Materials, Phys. Rev. Lett. **104**, 215902 (2010).

[61] A. N. Volkov, T. Shiga, D. Nicholson, J. Shiomi, and L. V. Zhigilei, Effect of bending buckling of carbon nanotubes on thermal conductivity of carbon nanotube materials, J. Appl. Phys. **111**, 053501 (2012).

[62] A. N. Volkov and L. V. Zhigilei, Heat conduction in carbon nanotube materials: Strong effect of intrinsic thermal conductivity of carbon nanotubes, Appl. Phys. Lett. **101**, 043113 (2012).

[63] J. Yang, M. Shen, Y. Yang, W. J. Evans, Z. Wei, W. Chen, A. A. Zinn, Y. Chen, R. Prasher, T. T. Xu, P. Keblinski, and D. Li, Phonon Transport Through Point Contacts Between Graphitic Nanomaterials, Phys. Rev. Lett. **112**, 205901 (2014).

[64] K. J. Zhang, A. Yadav, K. H. Kim, Y. Oh, M. F. Islam, C. Uher, and K. P. Pipe, Thermal and electrical transport in ultralow density single-walled carbon nanotube networks, Adv. Mater. **25**, 2926 (2013).

[65] Y. Yue, X. Huang, and X. Wang, Thermal transport in multiwall carbon nanotube buckypapers, Phys. Lett. A **374**, 4144 (2010).

[66] Y. Chalopin, S. Volz, and N. Mingo, Erratum: Upper bound to the thermal conductivity of carbon nanotube pellets [J. Appl. Phys. **105**, 084301 (2009)], J. Appl. Phys. **108**, 039902 (2010).

[67] S. Kumar and J. Y. Murthy, Interfacial thermal transport between nanotubes, J. Appl. Phys. **106**, 084302 (2009).

[68] W. J. Evans and P. Keblinski, Thermal conductivity of carbon nanotube cross-bar structures, Nanotechnology **21**, 475704 (2010).

[69] G.-J. Hu and B.-Y. Cao, Thermal resistance between crossed carbon nanotubes: Molecular dynamics simulations and analytical modeling, J. Appl. Phys. **114**, 224308 (2013).

[70] R. N. Salaway and L. V. Zhigilei, Molecular dynamics simulations of thermal conductivity of carbon nanotubes: Resolving the effects of computational parameters, Int. J. Heat Mass Transfer **70**, 954 (2014).

[71] L. Hu and A. J. H. McGaughey, Thermal conductance of the junction between single-walled carbon nanotubes, Appl. Phys. Lett. **105**, 193104 (2014).

[72] J. Tersoff, Empirical Interatomic Potential for Carbon, with Applications to Amorphous Carbon, Phys. Rev. Lett. **61**, 2879 (1988).

[73] J. E. Jones, On the determination of molecular fields. II. From the equation of state of a gas, Proc. R. Soc. Lon. Ser-A **106**, 463 (1924).

[74] S. Plimpton, Fast parallel algorithms for short-range molecular dynamics, J. Comput. Phys. **117**, 1 (1995).

[75] T. Schneider and E. Stoll, Molecular-dynamics study of a three-dimensional one-component model for distortive phase transitions, Phys. Rev. B **17**, 1302 (1978).

[76] P. K. Schelling, S. R. Phillpot, and P. Keblinski, Comparison of atomic-level simulation methods for computing thermal conductivity, Phys. Rev. B **65**, 144306 (2002).

[77] D. P. Sellan, E. S. Landry, J. E. Turney, A. J. H. McGaughey, and C. H. Amon, Size effects in molecular dynamics thermal conductivity predictions, Phys. Rev. B **81**, 214305 (2010).

[78] A. N. Volkov and L. V. Zhigilei, Mesoscopic interaction potential for carbon nanotubes of arbitrary length and orientation, J. Phys. Chem. C **114**, 5513 (2010).

[79] B. Gotsmann and M. A. Lantz, Quantized thermal transport across contacts of rough surfaces, Nat. Mater. **12**, 59 (2013).

[80] S. Cheng and M. O. Robbins, Defining contact at the atomic scale, Tribol. Lett. **39**, 329 (2010).

[81] Y. Mo, K. T. Turner, and I. Szlufarska, Friction laws at the nanoscale, Nature (London) **457**, 1116 (2009).

[82] Y. Mo and I. Szlufarska, Roughness picture of friction in dry nanoscale contacts, Phys. Rev. B **81**, 035405 (2010).

[83] J. Diao, D. Srivastava, and M. Menon, Molecular dynamics simulations of carbon nanotube/silicon interfacial thermal conductance, J. Chem. Phys. **128**, 164708 (2008).

[84] Y. Wang and P. Keblinski, Role of wetting and nanoscale roughness on thermal conductance at liquid-solid interface, Appl. Phys. Lett. **99**, 073112 (2011).

[85] J. C. Duda, T. S. English, E. S. Piekos, W. A. Soffa, L. V. Zhigilei, and P. E. Hopkins, Implications of cross-species interactions on the temperature dependence of Kapitza conductance, Phys. Rev. B **84**, 193301 (2011).

[86] Z.-Y. Ong and E. Pop, Molecular dynamics simulation of thermal boundary conductance between carbon nanotubes and SiO_2, Phys. Rev. B **81**, 155408 (2010).

[87] M. Hu, P. Keblinski, and P. K. Schelling, Kapitza conductance of siliconamorphous polyethylene interfaces by molecular dynamics simulations, Phys. Rev. B **79**, 104305 (2009).

[88] Z. Xu and M. J. Buehler, Strain controlled thermomutability of single-walled carbon nanotubes, Nanotechnology **20**, 185701 (2009).

[89] H. Zhu, Y. Xu, B.-L. Gu, and W. Duan, Robust linear dependence of thermal conductance on radial strain in carbon nanotubes, New J. Phys. **14**, 013053 (2012).

[90] A. N. Volkov and L. V. Zhigilei, Structural stability of carbon nanotube films: The role of bending buckling, ACS Nano **4**, 6187 (2010).

[91] L. V. Zhigilei, C. Wei, and D. Srivastava, Mesoscopic model for dynamic simulations of carbon nanotubes, Phys. Rev. B **71**, 165417 (2005).